visualized on 15% denaturing polyacrylamide gels using tricine buffer. All stable fragments larger than 2 kD were identified through NH_2-terminal sequencing and mass spectrometric analyses.

12. Mutant constructs were generated using standard polymerase chain reaction–based cloning strategy, and the identities of individual clones were verified through double-strand plasmid sequencing. The Smad-binding fragment from SARA (residues 665–721) was overexpressed in *Escherichia coli* strain BL21(DE3) as a glutathione S-transferase (GST)–fusion protein using a pGEX-2T vector (Pharmacia) and was purified by a glutathione sepharose 4B affinity column. The MH2 domain from Smad2 (residues 241–467) was overexpressed in a pET3d vector (Novagen). The soluble fraction of Smad2 MH2 in the *E. coli* lysate was purified by cation-exchange chromatography (SP-sepharose; Pharmacia) and gel-filtration chromatography (Superdex-75 column; Pharmacia). Equimolar amounts of GST-SARA SBD and Smad2 MH2 domain were mixed and incubated in 25 mM NaMES (pH 6.0), 50 mM NaCl, and 2 mM dithiothreitol (DTT). The complex was then passed through an cation-exchange column (SP-sepharose; Pharmacia), to which Smad2 MH2 domain binds avidly. GST-SARA SBD in isolation does not bind this column. Smad2 binding to the column has no effect on interaction with SARA. The bound complex was eluted from this column with 1 M NaCl and visualized on 15% SDS–polyacrylamide gel electrophoresis.
13. Proteins of the Smad2 MH2 domain and SARA SBD were individually purified and mixed in a 1:1 molar ratio. The final complex was concentrated and purified through gel-filtration chromatography (Superdex-75 column; Pharmacia). The concentration of the complex is ~20 mg/ml. Heavily twinned crystal clusters were grown at 4°C by the hanging-drop vapor-diffusion method by mixing the SARA-Smad2 protein complex with an equal volume of reservoir solution containing 100 mM Tris buffer (pH 8.5), 10% Dioxane (v/v), 2.0 M ammonium sulfate, and 10 mM DTT. Streak-seeding followed by three rounds of macro-seeding eventually generated crystals suitable for x-ray diffraction. The crystals, with a typical size of 0.1 mm by 0.1 mm by 0.4 mm, are in the trigonal space group P3121, with unit cell dimensions $a = b = 138.5$ Å, $c = 55.9$ Å, $\alpha = \beta = 90°$, $\gamma = 120°$, and contain two complexes in the asymmetric unit. Initial diffraction data were collected using an R-AXISIIC imaging plate detector mounted on a Rigaku 200HB generator. High-resolution data sets were collected at beamline X25 at the National Synchrotron Light Source (NSLS), Brookhaven National Laboratory. All data sets were collected under freezing conditions; crystals were equilibrated in a cryoprotectant buffer containing 100 mM Tris buffer (pH 8.5), 10% Dioxane (v/v), 2.0 M ammonium sulfate, and 20% glycerol, and were flash frozen under a –170°C nitrogen stream. The structure was primarily determined by molecular replacement using the software AMoRe [J. Navaza, *J. Acta Crystallogr. A* **50**, 157 (1994)]. The atomic coordinates of Smad4 MH2 were used for a rotational search against a 15–3.5 Å data set. The top 50 solutions from the rotational search were individually used for a subsequent translational search, which yielded one solution with a correlation factor of 20.8 and an *R*-factor of 52.4%. This solution was used to locate the second complex in the crystals. Together, these two solutions gave a combined correlation factor of 33.5 and an *R*-factor of 44%. This model was examined with the program O [T. A. Jones *et al.*, *Acta Crystallogr. A* **47**, 110 (1991)], and the Smad4 side chains were replaced with those of Smad2. Refinement by simulated annealing with the program X-PLOR (A. T. Brünger, Yale University), against a 3.0 Å native data set decreased the *R* factor and *R* free to 35% and 42%, respectively. Refinement against 2.2 Å resolution data allowed progressive identification of the SARA fragment. The final refined model contains two complexes of Smad2 (residues 263–456) and SARA (residues 669–709), and 243 water molecules. The NH_2- and COOH-terminal residues in Smad2 have no electron density, and we presume that these regions are disordered in the crystals. The two complexes in one asymmetric unit are similar with a rmsd of 0.79 Å for all aligned Cα atoms. We only report here one representative complex.
14. M. Miyaki *et al.*, *Oncogene* **18**, 3098 (1999).
15. Immunofluorescence was performed as described (9). Rhodamine-conjugated goat anti-mouse and fluorescein isothiocyanate (FITC)–conjugated goat anti-rabbit antibodies were purchased from Jackson ImmunoResearch Laboratories.
16. X. Chen, M. J. Rubock, M. Whitman, *Nature* **383**, 691 (1996).
17. Using a calcium phosphate–DNA precipitation method, HepG2 cells were transfected with the *Mix.2* ARE-luciferase reporter (*16*), FAST-2 [F. Liu *et al.*, *Mol. Cell. Biol.* **19**, 424 (1999)], with or without SARA and Smad2 constructs. Cells were treated with TGF'62 for 20 hours, and luciferase activity was determined.
18. X.-H. Feng and R. Derynck, *EMBO J.* **16**, 3912 (1997).
19. M. Huse, Y.-G. Chen, J. Massagué, J. Kuriyan, *Cell* **96**, 425 (1999).
20. R. Wieser, J. L. Wrana, J. Massagué, *EMBO J.* **14**, 2199 (1995).
21. S. Willis, C. M. Zimmerman, L. Li, L. S. Mathews, *Mol. Endocrinol.* **10**, 367 (1996).
22. X.-H. Feng, E. H. Filvaroff, R. Derynck, *J. Biol. Chem.* **270**, 24237 (1995).
23. A. A. Russo, P. D. Jeffrey, A. K. Patten, J. Massagué, N. P. Pavletich, *Nature* **382**, 325 (1996).
24. P. J. Klaulis, *J. Appl. Crystallogr.* **24**, 946 (1991).
25. A. Nicholls, K. A. Sharp, B. Honig, *Proteins Struct. Funct. Genet.* **11**, 281 (1991).
26. We thank H. Lewis for help with the X25 beamline at NSLS, S. Kyin for peptide sequencing and mass spectroscopic analysis, F. Hughson for critically reading the manuscript, L.-A. Swaby for technical support, M. Taga for help in early stages of this project, and E. Steckman for secretarial assistance. Supported by NIH grant CA85171 (Y.S.), Howard Hughes Medical Institutes (J.M.), Medical Research Council of Canada (J.L.W.), the Searle Foundation and the Rita Allen Foundation (Y.S.). Coordinates have been deposited with the Protein Data Bank (accession number 1DEV).

19 October 1999; accepted 19 November 1999

Generating Solitons by Phase Engineering of a Bose-Einstein Condensate

J. Denschlag,[1] J. E. Simsarian,[1] D. L. Feder,[1,2] Charles W. Clark,[1] L. A. Collins,[3] J. Cubizolles,[1,4] L. Deng,[1] E. W. Hagley,[1] K. Helmerson,[1] W. P. Reinhardt,[1,5] S. L. Rolston,[1] B. I. Schneider,[6] W. D. Phillips[1]

Quantum phase engineering is demonstrated with two techniques that allow the spatial phase distribution of a Bose-Einstein condensate (BEC) to be written and read out. A quantum state was designed and produced by optically imprinting a phase pattern onto a BEC of sodium atoms, and matter-wave interferometry with spatially resolved imaging was used to analyze the resultant phase distribution. An appropriate phase imprint created solitons, the first experimental realization of this nonlinear phenomenon in a BEC. The subsequent evolution of these excitations was investigated both experimentally and theoretically.

Ultimate control over a physical system can be achieved by precisely manipulating its quantum mechanical wave function, which fully characterizes its state. A BEC of a dilute gas (*1*) is particularly well suited for such manipulations because of its directly observable wave function: It has many identical atoms in the same quantum state, and it is large enough to be optically imaged.

We demonstrate two optical techniques to prepare and measure the phase of a BEC wave function. A chosen pattern of laser light imaged onto a condensate shapes its phase almost arbitrarily in two dimensions (*2–4*). Matter-wave interferometry (*5*) using optically induced Bragg diffraction (*6, 7*) is then used to analyze the spatial phase distribution by direct imaging (*8*). These methods are applied in experimental studies of a phenomenon in nonlinear atom optics (*9*), the propagation of solitons [solitary waves (*10*)] in a BEC. Three-dimensional (3D) numerical calculations agree well with and substantiate the experimental observations of soliton generation and propagation. Both reveal the rich dynamics of this nonlinear system, such as the formation of multiple solitons.

Theoretical background. Solitons are stable, localized waves that propagate in a nonlinear medium without spreading. They appear in diverse contexts of science and engineering, such as the dynamics of waves in shallow water (*11*), transport along DNA and other macromolecules (*12*), and fiber

[1]National Institute of Standards and Technology (NIST), Gaithersburg, MD 20899, USA. [2]University of Oxford, Parks Road, Oxford OX1 3PU, UK. [3]Theoretical Division, Mail Stop B212, Los Alamos National Laboratory, Los Alamos, NM 87545, USA. [4]Ecole Normale Superieure, 24 rue Lhomond, 75231 Paris, France. [5]Department of Chemistry, University of Washington, Seattle, WA 98195, USA. [6]Physics Division, National Science Foundation, Arlington, VA 22230, USA.

optic communications (*13*). Solitons may be either bright or dark, depending on the details of the governing nonlinear wave equation. A bright soliton is a peak in the amplitude; a dark soliton is a notch with a characteristic phase step across it.

A weakly interacting BEC obeys a nonlinear wave equation that supports solitons, as shown by recent theoretical studies (*14–17*). At zero temperature, this wave equation is known as the Gross-Pitaevskii equation (*18*),

$$i\hbar(\partial/\partial t)\psi = [-(\hbar^2/2M)\nabla^2 + V + g|\psi|^2]\psi \quad (1)$$

where ψ is the condensate wave function normalized to the number of atoms, V is the trapping potential, M is the atomic mass, $\hbar$ is the Planck constant divided by 2π and g describes the strength of the atom-atom interaction (*19*). Solitons propagate without spreading (dispersing) because the nonlinearity balances the dispersion; for Eq. 1, the corresponding terms are the nonlinear interaction $g|\psi|^2$ and the kinetic energy $-(\hbar^2/2M)\nabla^2$, respectively. Our sodium condensate only supports dark solitons because the atom-atom interactions are repulsive ($g > 0$).

A distinguishing characteristic of a dark soliton is that its speed is less than the Bogoliubov speed of sound, $v_0 = (gn/M)^{1/2}$ (*18*, *20*), where $n = |\psi_0|^2$ is the unperturbed condensate density. The soliton speed v_s can be expressed in terms of either the phase step δ ($0 < \delta \leq \pi$) or the soliton "depth" n_d, which is the difference between n and the density at the bottom of the notch (*14*, *15*):

$$v_s/v_0 = \cos(\delta/2) = [1 - (n_d/n)]^{1/2} \quad (2)$$

For $\delta = \pi$, the soliton has zero velocity, zero density at its center, a width on the order of the healing length $\xi = (2nMg/\hbar^2)^{-1/2}$ (*15*), and a discontinuous phase step. As δ decreases, the speed increases and approaches the speed of sound. The solitons become shallower and wider and have a more gradual phase step (*15*). They travel opposite to the direction of the phase gradient. Because a soliton has a characteristic phase step, optically imprinting a phase step on the BEC wave function should be a way to create a soliton.

Phase imprinting. We performed our experiments with a condensate having $\sim 2 \times 10^6$ sodium atoms in the $3S_{1/2}$, $F = 1$, $m_F = -1$ state, with no discernible thermal fraction (*7*). The condensate was held in a magnetic trap with trapping frequencies $\omega_x = \sqrt{2}\omega_y = 2\omega_z = 2\pi \times 28$ Hz. The Thomas-Fermi diameters (*18*) were 45, 64, and 90 μm, respectively. Initially the BEC, described by the ground-state solution of Eq. 1, had a uniform phase (*21*, *22*).

We modified the phase distribution of the BEC by exposing it to pulsed, off-resonant laser light with an intensity pattern $I(x,y)$ (Fig. 1). In this process, the atoms experience a spatially varying light-shift potential $U(x,y) = (\hbar\Gamma^2/8\Delta)[I(x,y)/I_0]$ and acquire a corresponding phase $\phi(x,y) = -U(x,y)T/\hbar$. Here Γ is the transition line width, I_0 is the saturation intensity, Δ is the detuning of the laser from the atomic resonance, and T is the laser pulse duration (*23*). We chose T to be short enough so that the atomic motion was negligible during the pulse (Raman-Nath regime). In this limit, the effect of the pulse can be expressed as a sudden phase imprint, which modifies the initial wave function: $\psi \rightarrow \psi \exp[i\phi(x,y)]$ (*24*).

Interferometry. We measured the imprinted phase distribution of the condensate wave function with a Mach-Zehnder matter-wave interferometer that makes use of optically induced Bragg diffraction (*25*, *26*). Our Bragg interferometer differs from previous ones in that we can independently manipulate atoms in the two arms (because of their large separation) and can resolve the output ports to reveal the spatial distribution of the condensate phase. In our interferometer, a Bragg pulse splits the initial condensate into two states, $|A\rangle$ and $|B\rangle$, differing only in their momenta (Fig. 2). After they spatially separate, the phase step (Fig. 1A) is imprinted on $|A\rangle$, while $|B\rangle$ is unaffected and serves as a phase reference. When recombined, they interfere according to their local phase difference. Where this phase difference is 0, atoms appear in port 1, and where it is π atoms appear in port 2. Imaging the density distributions of ports 1 and 2 displays the spatially varying phase (*27*). The image in Fig. 2 shows the output of the interferometer when a phase of π was imprinted on the upper half of $|A\rangle$ (*28*). The high-contrast "half moons" are direct evidence that we can control the condensate spatial phase distribution and, in particular, imprint the phase step appropriate for a soliton (*29*).

Soliton propagation. To observe soliton propagation, we did not use interferometry (*30*) but instead measured BEC density distributions with absorption imaging (*1*, *27*) after imprinting a phase step (*31*). Figure 3, A to E, shows the evolution of the condensate after the top half was phase-imprinted with $\phi_0 \approx 1.5\pi$, a phase for which we observed a single deep soliton (the reason for imprinting a phase step larger than π is discussed below). Immediately after the phase imprint, there is a steep phase gradient across the middle of the condensate such that this por-

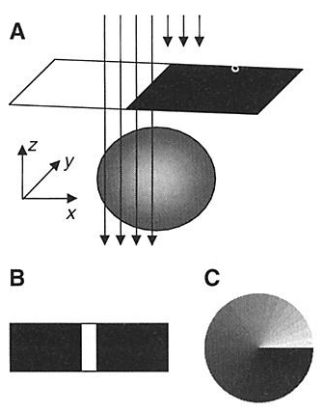

Fig. 1. (**A**) Writing a phase step onto the condensate. A far-detuned uniform light pulse projects a mask (a razor blade) onto the condensate. Because of the light shift, this imprints a phase distribution that is proportional to the light intensity distribution. A lens (not shown) is used to image the razor blade onto the condensate. The mask in (**B**) writes a phase stripe onto the condensate. The mask in (**C**) imprints an azimuthally varying phase pattern that can be used to create vortices.

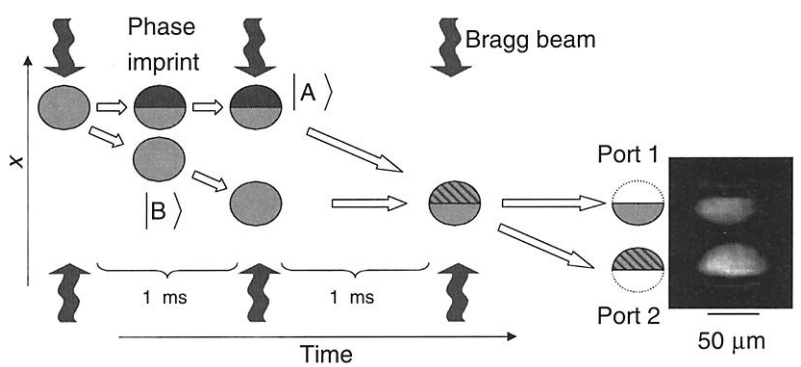

Fig. 2. Space-time diagram of the matter-wave interferometer used to measure the spatial phase distribution imprinted on the BEC. Three optically induced Bragg diffraction pulses (*7*) formed the interferometer. Each pulse consisted of two counterpropagating laser beams detuned by -2 GHz from atomic resonance (so that spontaneous emission is negligible), with their frequencies differing by 100 kHz. The first Bragg pulse had a duration of 8 μs and coherently split the condensate into two components $|A\rangle$ and $|B\rangle$ with equal numbers of atoms; $|A\rangle$ remained at rest and $|B\rangle$ received two photon recoils of momentum. When they were completely separated, we applied the 500-ns phase imprint pulse to the top half of $|A\rangle$, which changed the phase distribution of $|A\rangle$ while $|B\rangle$ served as a phase reference. A second Bragg pulse (duration 16 μs), 1 ms after the first pulse, brought $|B\rangle$ to rest and imparted two photon momenta to $|A\rangle$. When they overlapped again, 1 ms later, a third pulse (duration 8 μs) converted their phase differences into density distributions at ports 1 and 2. The image shows the output ports 1 and 2 as seen when we imprinted a phase step of π (*29*).

tion has a large velocity in the $+x$ direction. This velocity, which can be understood as arising from the impulse imparted by the optical dipole force, results in a positive density disturbance that travels at or above the speed of sound. A dark notch is left behind; this is a soliton moving slowly in the $-x$ direction (opposite to the direction of the applied force).

We have numerically solved Eq. 1 in three dimensions through the application of real-space product formulas (*32*) and by using a discrete variable representation of the wave function (*33*) based on Gauss-Chebyshev quadrature with 50 to 400 spatial grid points in each dimension; in the latter approach, the time dependence of the solution was obtained by Runge-Kutta integration. Figure 3, F to J, shows the results of the simulations where the experimental phase imprint is approximated as $\phi(x,y) = (\phi_0/2)[1 + \tanh(x/l)]$, where $\phi_0 = 1.5\pi$, and $l = 2$ μm corresponds to an imprinting resolution of ~4.4 μm (*27, 34*). The calculated and experimental images are in very good agreement.

A striking feature of the images is the curvature of the soliton. This curvature arises from the 3D geometry of the trapped condensate and occurs for two reasons. First, the speed of sound v_0 is largest at the trap center, where the density is greatest, and decreases toward the condensate edge. Second, as the soliton moves into regions of lower condensate density, we find numerically that the density at its center ($n - n_d$) approaches zero, δ approaches π, and v_s decreases to zero before reaching the edge. The soliton stops because its depth n_d, rather than its phase offset δ, appears to be a conserved quantity in a nonuniform medium.

Soliton speed. The subsonic propagation speed of the notches seen in Fig. 3 shows that they are solitons and not simply sound waves. To determine this speed, we measured the distance after propagation between the notch and the position of the imprinted phase step along the direction indicated in Fig. 3H. Because the position of our condensate varied randomly from one shot to the next (presumably because of stray, time-varying fields), we could not always apply the phase step at the center. A marker for the location of the initial phase step is the intersection of the soliton with the condensate edge, because at this point the soliton has zero velocity. By using images taken 5 ms after the imprint, at which time the soliton had not traveled far from the BEC center, we obtained a mean soliton speed of 1.8 ± 0.4 mm/s (*35*). This value is significantly less than the mean Bogoliubov speed of sound, $v_0 = 2.8 \pm 0.1$ mm/s. From the propagation of the notch in the numerical simulations (Fig. 3, F to J), we obtained a mean soliton speed, $v_s = 1.6$ mm/s, in agreement with the experimental value. The experimental uncertainty is mainly due to the difficulty in determining the position of the initial phase step.

We can also compare the results of the numerical 3D solutions of Eq. 1 to the analytical predictions of Eq. 2, which describes a traditional dark soliton in a homogeneous, 1D geometry. We calculated the soliton speed using a local density approximation in Eq. 2 [$n = |\pi_0(r)|^2$, where $\pi_0(r)$ is the ground-state solution of Eq. 1] from either the phase or depth of the solitons obtained in the 3D simulations. In every case examined, this speed is in excellent agreement with the results of 3D numerical simulations.

Figure 4 shows the theoretical density and phase profile along the x axis through the center of the condensate 5 ms after the $\phi_0 = 1.5\pi$ phase imprint (Fig. 3H). The dark soliton notch and its phase step are centered at $x = -8$ μm. This phase step, $\delta = 0.58\pi$ is less than the imprinted phase of 1.5π. The difference is caused by the mismatch between the phase imprint and the phase and depth of the soliton solution of Eq. 1: Our imprinting resolution (*27*) is larger than the soliton width, which is on the order of the healing length ($\xi \approx 0.7$ μm), and we do not control the amplitude of the wave function. The mismatch produces features in addition to the deep soliton, such as a shallow dark soliton at $x = -14$ μm moving to the left and other excitations near $x = 20$ μm moving rapidly to the right. Most of these features are not well resolved in the experimental images (Fig. 3, A to E). We observed both experimentally and theoretically that when the imprinted phase step is increased, the weak soliton on the left becomes deeper; when the phase step is lowered, both solitons become shallower and propagate faster.

We could avoid the uncertainty in the position of the initial phase step and improve our measurement of the soliton speed by replacing the step mask (Fig. 1A) with a thin slit (Fig. 1B). The thin slit produced a stripe of light with a Gaussian profile ($1/e^2$ full width ≈ 15 μm). With this stripe in the center of the condensate, numerical simulations predict the generation of solitons that propagate symmetrically outward. We selected experimental images with solitons symmetrically located about the middle of the condensate and measured the distance between them. Figure 5A shows the separation of the pair of solitons as a function of time. For a small phase imprint of $\phi_0 \approx 0.5\pi$ at Gaussian maximum, we observed solitons moving at the Bogoliubov speed of sound within experimental uncertainty. For a larger phase imprint of $\phi_0 \approx 1.5\pi$, we observed a much slower soliton propagation, in agreement with numerical simulations. An even larger phase imprint

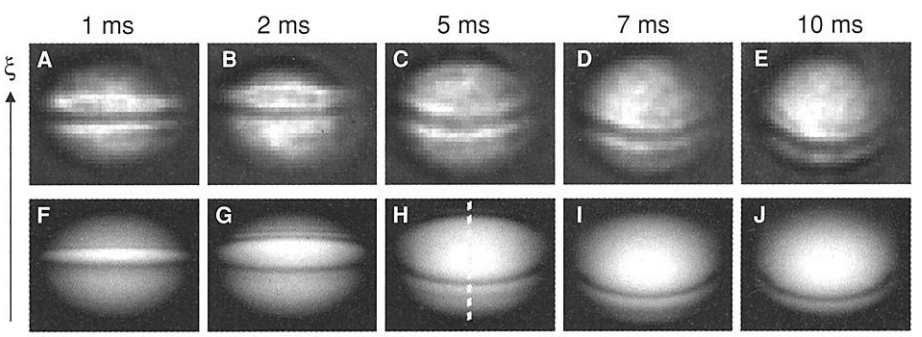

Fig. 3. Experimental (**A** to **E**) and theoretical (**F** to **J**) images of the integrated BEC density for various times after we imprinted a phase step of ~1.5π on the top half of the condensate with a 1-μs pulse. The measured number of atoms in the condensate was 1.7 (±0.3) × 10^6, and this value was used in the calculations. A positive density disturbance moved rapidly in the $+x$ direction, and a dark soliton moved oppositely at significantly less than the speed of sound. Because the imaging pulse (*27*) is destructive, each image shows a different BEC. The width of each frame is 70 μm.

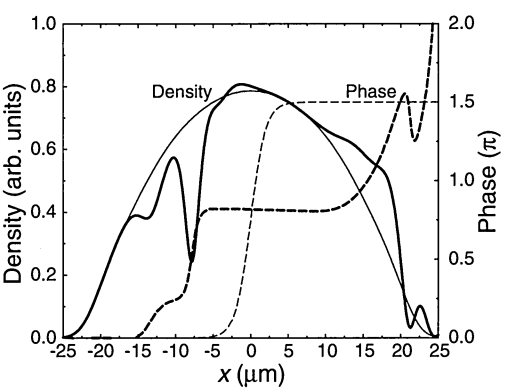

Fig. 4. Calculated density and phase along the x axis (dashed line in Fig. 3H) at 0 ms (thin lines) and at 5 ms (thick lines) after applying a phase step imprint of 1.5π. The soliton located at $x = -8$ μm has a phase step of 0.58π and a speed of 1.61 mm/s, which is much less than that of sound.

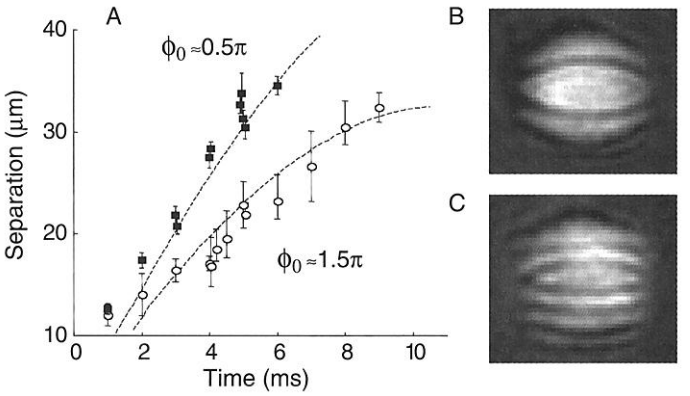

Fig. 5. (**A**) Plot of separation versus time for two oppositely propagating solitons after a phase imprint in the form of a stripe. For a small phase imprint ($\phi_0 \approx 0.5\pi$, squares), the solitons move at almost the local speed of sound. For a larger phase imprint ($\phi_0 \approx 1.5\pi$, circles), they are much slower. The dashed lines are from numerical simulations, from which we extract speeds for the corresponding solitons of 2.56 mm/s ($\phi_0 = 0.5\pi$) and 1.75 mm/s ($\phi_0 = 1.5\pi$) at 4 ms. (**B**) The condensate 6 ms after a stripe phase imprint of $\phi_0 \approx 1.5\pi$. (**C**) For a larger phase imprint of $\phi_0 \approx 2\pi$ many solitons appeared.

generates many solitons (Fig. 5C).

The lower theoretical curve in Fig. 5A shows that the speed of the corresponding solitons (the slope of the curve) approaches zero at a separation of ~33 μm before they reach the edge of the condensate (whose Thomas-Fermi diameter is 45 μm). This result follows directly from Eq. 2. Assuming a constant soliton depth n_d and working in the Thomas-Fermi limit, the derivative of v_s with respect to time yields the equation of motion $dv_s/dt \equiv d^2x_s/dt^2 = -\omega^2 x_s/2$. Thus, the soliton in a 1D trap should oscillate harmonically with a frequency $\omega_s = \omega/\sqrt{2}$, smaller than the trap frequency ω. Previous calculations have also found this behavior (*17*). In our system, therefore, the soliton should stop after one-quarter of the oscillation time, $(\pi/2)(\sqrt{2}/\omega_x)$ ms, which is in agreement with our 3D simulations. The 3D calculations, however, indicate that the soliton does not oscillate back after stopping, but instead breaks up, forming vortices that migrate to the BEC surface and disappear.

Future directions. The optical phase imprinting and matter-wave interferometry techniques presented here are new control and analysis tools for wave function engineering of Bose-Einstein condensates. For example, the interferometer might also be used to study randomness in the evolution of the condensate phase (phase diffusion). Our optical imprinting techniques could be extended to the control of wave function amplitude, with the use of near-resonant laser frequencies to induce absorption. The probability of removing atoms from the condensate would then be proportional to the local intensity of the laser beam, allowing us to tailor the density distribution of the BEC in addition to its phase.

Future avenues for research include studies of soliton stabilities and the interactions between solitons, as well as other nonlinear dynamics of condensates. Another possibility is the use of optical phase imprinting to create quantized vortices in a BEC (*2*). The 2π phase winding of the vortex wave function around its core can be imprinted by imaging an intensity pattern with a linear azimuthal dependence (Fig. 1C). Quantized vortices in a BEC are a manifestation of superfluidity and have recently been observed in a two-component condensate (*4*) and a condensate in a rotating trap (*36*). We note that a group in Hannover, Germany, has independently studied solitons in a BEC using optical phase imprinting (*37*).

References and Notes

1. M. H. Anderson, J. R. Ensher, M. R. Matthews, C. E. Wieman, E. A. Cornell, *Science* **269**, 198 (1995); K. B. Davis *et al.*, *Phys. Rev. Lett.* **75**, 3969 (1995); C. C. Bradley, C. A. Sackett, R. G. Hulet, *Phys. Rev. Lett.* **78**, 985 (1997); see also C. C. Bradley, C. A. Sackett, J. J. Tollett, R. G. Hulet, *Phys. Rev. Lett.* **75**, 985 (1995).
2. The optical phase imprinting technique has been independently proposed by L. Dobrek *et al.* [*Phys. Rev. A* **60**, R3381 (1999)].
3. A different phase-engineering scheme using a two-component BEC was recently developed [M. R. Matthews *et al.*, *Phys. Rev. Lett.* **83**, 3358 (1999); J. Williams and M. Holland, *Nature* **401**, 568 (1999); see also (*4*)].
4. M. R. Matthews *et al.*, *Phys. Rev. Lett.* **83**, 2498 (1999).
5. P. R. Berman, Ed., *Atom Interferometry* (Academic Press, Cambridge, 1997); C. S. Adams, M. Sigel, J. Mlynek, *Phys. Rep.* **240**, 143 (1994).
6. P. J. Martin, B. G. Oldaker, A. H. Miklich, D. E. Pritchard, *Phys. Rev. Lett.* **60**, 515 (1988).
7. M. Kozuma *et al.*, *Phys. Rev. Lett.* **82**, 871 (1999).
8. Recent experiments also demonstrated spatial phase measurements by direct imaging using interferometry with two different internal states (*4*).
9. G. Lens, P. Meystre, E. W. Wright, *Phys. Rev. Lett.* **71**, 3271 (1993); L. Deng *et al.*, *Nature* **398**, 218 (1999).
10. In this article, we do not distinguish between the terms "soliton" and "solitary wave" because we do not investigate their collisional properties (*13*).
11. R. K. Bullough, in *Solitons*, M. Lakshmanan, Ed. (Springer-Verlag, Berlin, 1988), pp. 150–281.
12. M. Peyrard, Ed., *Molecular Excitations in Biomolecules* (Springer-Verlag, New York, 1995).
13. A. Hasegawa, *Optical Solitons in Fibers* (Springer-Verlag, Berlin, ed. 2, 1990); J. K. Taylor, Ed., *Optical Solitons Theory & Experiment* (Cambridge Univ. Press, New York, 1992).
14. W. P. Reinhardt and C. W. Clark, *J. Phys. B* **30**, L785 (1997); W. P. Reinhardt, in *Tunneling in Complex Systems*, S. Tomsovic, Ed. (World Scientific, Singapore, 1998), pp. 277–326.
15. A. D. Jackson, G. M. Kavoulakis, C. J. Pethick, *Phys. Rev. A* **58**, 2417 (1998).
16. R. Dum, J. I. Cirac, M. Lewenstein, P. Zoller, *Phys. Rev. Lett.* **80**, 2972 (1998); V. M. Pérez-García, H. Michinel, H. Herrero, *Phys. Rev. A* **57**, 3837 (1998); O. Zobay, S. Pötting, P. Meystre, E. M. Wright, *Phys. Rev. A* **59**, 643 (1999); P. O. Fedichev, A. E. Muryshev, G. V. Shlyapnikov, *Phys. Rev. A* **60**, 3220 (1999).
17. A. E. Muryshev, H. B. van Linden van den Heuvell, G. V. Shlyapnikov, *Phys. Rev. A* **60**, R2665 (1999); T. Busch and J. Anglin, Los Alamos National Laboratory e-print cond-mat/9809408 (1998).
18. F. Dalfovo, S. Giorgini, L. P. Pitaevskii, S. Stringari, *Rev. Mod. Phys.* **71**, 463 (1999).
19. The coupling constant g is given by $g = 4\pi\hbar^2 a/M$, where a = 2.75 nm [E. Tiesinga *et al.*, *J. Res. Natl. Inst. Stand. Technol.* **101**, 505 (1996)] is the scattering length of sodium for the $F = 1$, $m_F = -1$ state.
20. M. R. Andrews *et al.*, *Phys. Rev. Lett.* **79**, 553 (1997).
21. E. W. Hagley *et al.*, *Phys. Rev. Lett.* **83**, 3112 (1999).
22. J. Stenger *et al.*, *Phys. Rev. Lett.* **82**, 4569 (1999).
23. For the $3S_{1/2}, F = 1 \rightarrow 3P_{3/2}$ sodium transition at 589 nm, $\Gamma/2\pi$ = 10 MHz, and I_0 = 9.3 mW/cm² is the effective saturation intensity for linearly polarized light detuned far from resonance compared with the relevant upper-state hyperfine splitting (50 MHz). In our case, $\Delta/2\pi = -0.6$ GHz and $T \sim 1$ μs. The probability of spontaneous emission during the pulse is small.
24. Diffraction with an optical standing wave can also be interpreted as a sinusoidal phase imprint.
25. Y. Torii *et al.*, Los Alamos National Laboratory e-print cond-mat/9908160 (1999).
26. D. M. Giltner, R. W. McGowan, S. A. Lee, *Phys. Rev. Lett.* **75**, 2638 (1995).
27. The condensate was imaged with a probe along the direction of the phase imprinting beam. We used absorption imaging with a 5-μs light pulse (intensity ~170 mW/cm²) detuned 15 MHz from resonance (*7*). This produced high-contrast images that made use of nearly the full dynamic range of the charge-coupled device camera. The images gave a reliable measurement of the soliton location. We measured a combined resolution of the phase imprinting and the imaging optics to be 7 μm, whereas the diffraction limit of the phase imprinting optics is 2.5 μm. We define the resolution as the distance in which the light intensity falls from 90% to 10% of its full value.
28. For Fig. 2, we released the BEC from the magnetic trap 500 μs after the first interferometer pulse.
29. Because of mirror vibrations, our interferometer experiences random phase variations between the interferometer arms from one shot to the next. Despite this limitation, we can still unambiguously identify phase step imprints of π because only then can high-contrast "half moon" images be obtained. In that case we can choose an image for which the random phase is zero, as in Fig. 2. By mechanically stabilizing the interferometer, the global random phase can be controlled and the interferometer could then be used more quantitatively.
30. The asymmetric nature of our interferometer does not lend itself to measuring the phase of a trapped condensate after long propagation times. The differential velocity between the interferometer arms, which results from the action of the trapping potential, leads to fringes at the output.
31. The condensate was released from the magnetic trap 1 ms before being imaged. Expansion of the released BEC during that time was negligible.
32. L. A. Collins, J. D. Kress, R. B. Walker, *Comput. Phys. Commun.* **114**, 15 (1998).
33. B. I. Schneider and D. L. Feder, *Phys. Rev. A* **59**, 2232 (1999).
34. The 4.4-μm resolution (*27*) is centered within the range of the 2.5-μm diffraction limit and the measured 7-μm upper limit. Simulations with a phase-imprinting resolution of 7 μm yielded results that are qualitatively similar to those with the 4.4-μm calculation but do not agree as well with the experimental observations.
35. All uncertainties reported in this article are 1 standard deviation combined statistical and systematic uncertainties.

36. K. W. Madison *et al.*, preprint available at http://xxx.lanl.gov/abs/cond-mat/9912015.
37. S. Burger *et al.*, preprint available at http://xxx.lanl.gov/abs/cond-mat/9910487.

38. We thank K. Burnett, M. A. Edwards, and K. Jones for discussions. Supported in part by the U.S. Office of Naval Research and NASA. J.D., J.E.S., and W.P.R. acknowledge support from the Alexander von Humboldt Foundation, a NIST–National Research Council fellowship, and NSF, respectively.

15 October 1999; accepted 2 December 1999

REPORTS

Equilibrium Regained: From Nonequilibrium Chaos to Statistical Mechanics

David A. Egolf

Far-from-equilibrium, spatially extended chaotic systems have generally eluded analytical solution, leading researchers to consider theories based on a statistical rather than a detailed knowledge of the microscopic length scales. Building on the recent discovery of a separation of length scales between macroscopic behavior and microscopic chaos, a simple far-from-equilibrium spatially extended chaotic system has been studied computationally at intermediate, coarse-grained scales. Equilibrium properties such as Gibbs distributions and detailed balance are recovered at these scales, which suggests that the macroscopic behavior of some far-from-equilibrium systems might be understood in terms of equilibrium statistical mechanics.

Statistical mechanics describes the macroscopic physical properties of matter through a probabilistic, rather than a detailed, knowledge of the microscopic dynamics and has been applied successfully to a wide variety of equilibrium systems, from simple molecular gases to white dwarf stars. It has provided a theoretical understanding of the phases of matter, the transitions between phases, and the deep property of universality that unifies the descriptions of continuous transitions in systems that are physically quite distinct (for example, magnets and gases). In nature, however, many systems are not in equilibrium, including, for example, large-scale flows in the atmosphere, the evolution of ecological systems, and the transport of energy in cells. None of these situations can be understood with equilibrium statistical mechanics.

Although theory has been developed to extend equilibrium statistical mechanics to systems only slightly perturbed away from equilibrium (for which the evolution of the system is well-approximated with only linear terms), in deterministic systems driven far from equilibrium (where nonlinearities are important) theoretical progress has been limited to "simple" situations, such as the onset of symmetry breaking, the stability of perfect patterns, and the motions of single topological defects in perfect patterns (*1*). Theorists have not yet developed an understanding of the intriguing phenomenon of "spatiotemporal chaos" (or spatially extended chaos) that is typically characterized by disordered arrays of defects, patches of uncorrelated regions, and a chaotic dynamics that persists indefinitely (*2*). This remarkable behavior has been found in large, deterministic, far-from-equilibrium systems as varied as convecting horizontal fluid layers (*3*), chemical reaction-diffusion systems (*4*), colonies of microorganisms (*5*), and fibrillating heart tissue (*6*). These disparate systems often display strikingly similar macroscopic features (such as locally ordered striped or hexagonal patterns and dislocation, spiral, and target defects) and behavior (for example, dramatic qualitative changes in response to modifications of experimental parameters reminiscent of phase transitions in equilibrium systems). Such behavior within a system and the similarities between different systems beg the question of whether one can construct a statistical, predictive theory of phases and transitions in these chaotic, far-from-equilibrium systems.

At first glance, far-from-equilibrium, strongly dissipative, deterministic systems may appear to have little in common with equilibrium systems; for example, at the detailed level, these systems do not have the benefit of tending toward the minimum of a free-energy functional, do not have a Gibbsian distribution of states, and do not allow the calculational technique of averages over noise terms. However, several experimental and computational studies have explored the similarities in the behaviors of these systems and the behaviors of equilibrium systems. A particular focus has been the possibility of phase transition–like behavior in these systems (*4*, *7*–*11*). The data reported here uncover a deeper level of similarity and suggest the possibility of salvaging much of the framework of equilibrium statistical mechanics. In particular, large-scale computational studies of a simple, large, chaotic, far-from-equilibrium system demonstrate that several cornerstones of equilibrium statistical mechanics—ergodicity, detailed balance, Gibbs distributions, partition functions, and renormalization group flows of coupling constants—are recovered at a coarse-grained scale.

In analogy to the simple explorations of equilibrium statistical mechanics with the Ising model, one of the simplest spatially extended chaotic systems was used as a test bed (*12*). This system, a coupled map lattice (CML) first studied by Miller and Huse (*8*), consists of a set of scalar variables $u^t_{\vec{x}}$ at integer time t on a square two-dimensional spatially periodic $L \times L$ grid with positions indicated by $\vec{x} = a\hat{x} + b\hat{y}$, where a and b are integers and $\hat{x}$ and $\hat{y}$ are the unit vectors of the two-dimensional lattice. The rule for updating the variables from time t to $t + 1$ is

$$u^{t+1}_{\vec{x}} = \phi(u^t_{\vec{x}}) + g\sum_{\vec{y}(\vec{x})}[\phi(u^t_{\vec{y}}) - \phi(u^t_{\vec{x}})] \tag{1a}$$

where g indicates the strength of the spatial coupling, and $\vec{y}(\vec{x})$ denotes nearest neighbors of site $\vec{x}$. The chaotic local map $\phi(u)$ is given by

$$\phi(u) = \begin{cases} -3u - 2 & -1 \le u \le -\frac{1}{3} \\ 3u & -\frac{1}{3} < u < \frac{1}{3} \\ -3u + 2 & \frac{1}{3} \le u \le 1 \end{cases} \tag{1b}$$

This CML exhibits chaotic, spatially disordered dynamics for values of g at least within the range [0, 0.25]. Miller and Huse (*8*) reported that at $g_c \approx 0.2054$, this system undergoes a paramagnetic-to-ferromagnetic transition exhibiting a number of features in common with the equilibrium transition in the Ising ferromagnet (*13*).

To study the statistical bulk properties of spatially extended chaotic states ["extensive chaos" (*1*, *14*)], the "thermodynamic limit" of systems approaching infinite size was taken. O'Hern *et al.* (*15*) demonstrated that the behavior of Eq. 1 can be considered extensive for system sizes as small as $L \approx 9$. Results reported here were obtained for system sizes ranging from 1×1 to 1024×1024 over times as large as 10^{10} iterations (after typically 10^6 iterations of transient), often averaged over ensembles of up to 256 systems with identical parameters but differing initial conditions [with each site $u^{t=0}_{\vec{x}}$ initialized to a

Center for Nonlinear Studies (MS B258), Theoretical Division and Condensed Matter and Thermal Physics, Los Alamos National Laboratory, Los Alamos, NM 87545, USA. E-mail: egolf@cnls.lanl.gov